

# Study on laser shock modulation of melt pool in Laser Additive Manufacturing of FeCoCrNi High-Entropy Alloys

Heng Lu <sup>a</sup>, Xiaohan Zhang <sup>a</sup>, Jian Liu <sup>a</sup>, Shusen Zhao <sup>b</sup>, Xuechun Lin <sup>b</sup>, Hui Li <sup>a</sup>, Yaowu Hu <sup>a,\*</sup>

<sup>a</sup> The Institute of Technological Sciences, Wuhan University, Wuhan, 430072, China

<sup>b</sup> The Institute of Semiconductors, Chinese Academy of Sciences, Beijing, 100083, China

## Abstract:

With growing interest in Laser Additive Manufacturing (LAM) of High-entropy alloys (HEAs) during most recent years, compositional elements design and process strategies innovation are primary methods to overcome undesirable microstructures and defects. Here we propose a new approach, a novel real-time laser shock modulation of melt pool (LSMMP) to obtain melt pool modifications for yielding HEAs with desired characteristics. LSMMP utilizes a pulsed laser shocking a liquid melt pool caused by a continuous wave laser, enabling non-destructive and real-time modulations for high-performance HEAs. The numerical simulation reveals the convection mechanism of the melt pool in the LSMMP process, and the intervention of the pulsed laser promotes melt pool flow type to convert the Marangoni effect into a multi-convective ring, which accelerates melt pool flow and inhibits columnar crystal growth. Experimental results show the evolution law of the microstructure in the LSMMP process. The microstructure of CrFeCoNi HEAs undergoes a Columnar-Equiaxed Transition (CET), and higher hardness is obtained. Laser shock is demonstrated to be an effective in-situ modulative tool for controlled additive manufacturing.

**Keywords:** Laser shock; High-entropy alloys; Melt pool; Laser Additive Manufacturing

---

\* Corresponding author: Yaowu Hu. E-mail address: [yaowuhu@whu.edu.cn](mailto:yaowuhu@whu.edu.cn).

## 1. Introduction

To create a new type of material, Yeh et al. [1] broke the traditional design concept of a single metal as the main element and designed High-Entropy Alloys (HEAs) with excellent performance. It has brought a new dawn for the development of new alloy systems, which has received extensive attention in many fields of basic research and engineering manufacturing. Typical metallurgical defects such as porosity, pores, and segregation in conventional as-casted HEAs affected the final properties, which limited the potential application of HEAs. Since Brief et al.[2] firstly used Laser Additive Manufacturing (LAM) to obtain HEAs with better mechanical properties than as-casted samples, and demonstrated the feasibility of LAMed HEAs. Moghaddam et al.[3] presented a comprehensive review of LAMed HEAs. It shows that various parts with smooth and bright surfaces can be successfully manufactured using LAM. The many advantages of LAM such as addition of beneficial elements, regulation of process parameters, and selection of appropriate technologies are used to address these defects. More scholars such as Li et al. [4] have transferred the research focus from FeCoCrNi-based HEAs to performance by adding novel materials. Zhou et al. [5] fabricated carbon-containing FeCoCrNiC<sub>0.05</sub> HEAs by Selective Laser Melting (SLM). The structure is a single face-centered cubic (FCC) without carbide phases, and the carbon distribution in the samples prepared under optimal parameters is uniform. The pre-mixed powder approach also developed LAM technology to non-metallic materials, Hu et al.[6] enhanced plasticity of Zr-based Bulk Metallic Glass (BMG) by adding higher thermal diffusivity of Nb element. Zhu et al.[7] manufactured near-fully dense CoCrFeNiMn HEAs by regulating and controlling laser power density, and an outstanding combination of high strength and excellent ductility compared to those fabricated by conventional methods was achieved in the as-built samples. Peyrouzet et al.[8] obtained Al<sub>0.3</sub>CoCrFeNi HEAs with a tensile

strength up to 896 MPa and yield strength of 730 MPa by changing the aluminum content, which was greatly improved for SLMed HEAs compared with as-cast or wrought counterparts. However, to realize the promising future of LAMed HEAs, not only extensive materials with new geometries need to be developed, but also novel AM routes are required to broaden the fabrication capability.

The extreme thermal cycle of the melt pool during the LAM process also brings many hazards such as pores, cracks, and large grains. Zhang et al.[9] observed cracks in the CoCrFeNiMn HEAs samples under different scanning strategies, and Niu et al.[10] also found the same result. Many scholars have joined the effort to solve this problem. For example, Jiang et al. [11] showed that 5% Fe-based amorphous reinforced AlCoCrFeNi HEAs reduced the grain diameter and eliminates the presence of texture, and the anisotropy of the specimen was reduced. In addition, the cooling rate of the melt pool, a critical factor, directly affects the recrystallization process which also leads to HEAs with different properties. Li et al.[12] revealed the formation mechanism of microstructures in HEAs rapidly cooled to room temperature at nanoscale through Molecular dynamics (MD) simulation. Most HEAs prepared by Laser Melting Deposition (LMD) exhibit typical columnar dendrites. This is because the growth rate of LMD is lower than that of the SLM process, so that equiaxed crystals cannot be achieved. Tong et al.[13] found the microstructure of the SLMed CoCrFeNiMn HEAs is mainly columnar crystals inside the melt pool. Knowles et al.[14] used a range of annealing processes after Direct Metal Laser Sintering (DMLS) and Li et al.[4] applied the Hot isostatic pressing (HIP) after SLM to change the microstructures, which are typical cumbersome and detrimental to the continuity of the AM process. However, Tong et al.[15] found that applying different process parameters such as laser power and scanning speed in the LAM process can directly obtain different microstructures. The ratio of the temperature gradient ( $G$ ) and solidification velocity ( $R$ ) inside the melt pool are the

dominant factors in Columnar-Equiaxed Transition (CET).

In-situ modification of the melt pool to get better structures in the LAM process is therefore particularly important. Laser Shock Peening (LSP) is an advanced technology that not only induces high compressive stress on the surface of metal components and structures but also can control structures at the micro and nano levels. For example, Hu et al.[16, 17] realized ultrafast direct fabrication of surface metallic nanoarrays by LSP. Here a novel synchronous Laser Shock Modulation of Melt Pool (LSMMP) method was proposed to enhance melt pool convections and inhibit columnar crystal growth via an additional second pulsed laser in the LAM process. It extends the effort of Tong et al.[15] who used the LSP as a post-processing treatment to modification to improve the LAMed HEAs. Although pulsed laser is widely used in material properties strengthening. To our knowledge, there are not any researches on a synchronous hybrid additive manufacturing process with laser shocking of melt pool to directly interfere the recrystallization process. In this paper, the action mechanism of LSMMP was studied by combined experiments and numerical simulations. We reveal the convection mechanism inside the melt pool under the action of sub-10 nanosecond Joule-scale pulsed laser. The microstructure evolution law of HEAs produced by LSMMP was discussed to demonstrate the ultrafast real-time interference capability of LSMMP in metal laser additive manufacturing.

## 2. Material and Methods

### 2.1. Materials and Experiment

The LSMMP integrates a pulsed laser into a melt pool of liquid HEAs produced by a continuous wave (CW) laser as shown in Fig.1 (a). A size of 30 mm × 30 mm × 1 mm 45# carbon steel (The main component is iron and contains the following elements: C: 0.42-0.5%; Si: 0.17~0.37%; Mn:

0.50~0.80%; P:  $\leq 0.035\%$ ; S:  $\leq 0.035\%$ ; Cr:  $\leq 0.25\%$ ; Ni :  $\leq 0.25\%$ ; Cu:  $\leq 0.25\%$ .) was cleaned with ethanol solution after polishing to ensure cleanliness. The experimental material adopts the equiatomic CrFeCoNi powder prepared by vacuum atomization. The particle size is 15~45 $\mu\text{m}$ . It has good fluidity and sphericity. The powder morphology and composition analysis are shown in Fig.1 (b) and (c). The single thickness of CoCrFeNi powder bed is about 1mm. Experimental equipment includes a 1kW continuous wave (CW) fiber laser (Shenzhen Chuangxin Laser Co., Ltd.) and a sub-10 nanosecond Joule-scale pulsed laser. The SLM process was carried out in a high-purity argon atmosphere with a gas supply rate of 3 L/min. The process parameters are laser power of 800 W, laser scanning speed of 20 mm/s, and spot diameter of 3 mm. The pulsed laser process parameters are laser energy of 3J, pulse width of 10 ns, repetition frequency of 10Hz, and spot diameter of 2 mm. The relevant laser energy density (LED) is defined as  $S_{LED}=P/A$ , where  $P$  is the laser energy, and  $A$  is the laser spot area. The CW laser beam is perpendicular to the substrate, and the pulsed laser beam deviates from the vertical by  $-10^\circ$ .

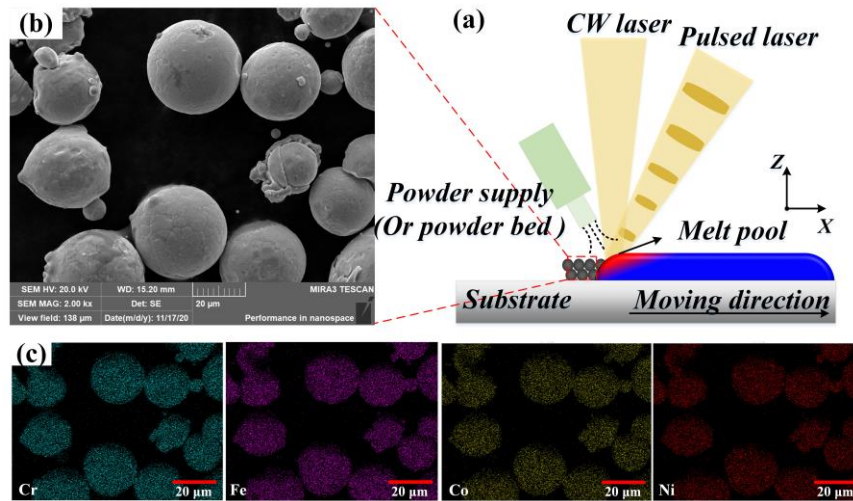


**Fig.1.** (a) Experimental schematic diagram, (b) the SEM image of CrFeCoNi powder, and (c) the EDS analysis of CrFeCoNi powder.

## 2.2. Characterization Methods

Different samples were tested from these aspects: process, microstructure, and phase composition

and mechanical properties. A Chronos1.4 high-speed camera (Kron Technologies, Canada) was used to monitor the manufacturing process and the NewView™ 9000 Series white light interference 3D profiler (ZYGO, The United States) was used to measure the profile of the sample. The samples were corroded by aqua regia (hydrochloric acid: nitric acid=3:1) for 60 seconds after polishing and cleaning of the cross-section. The microstructure and the Energy-dispersive Spectroscopy (EDS) tests utilized the BX51 optical microscope (OLYMPUS, Japan) and the MIRA3 scan electron microscope (SEM) (Tescan, The Czech Republic). To understand the phase composition of the original CoCrFeNi powder and the samples, the D8 ADVANCE X-ray diffractometer (XRD) (Bruker, The German) was used. The scanning angle is 20-90 ° and the scanning speed was 5 °/min. iNano nanoindenter (KLA-Tencor, The United States) with a load of 50 mN and diamond indenter tip were used to obtain the mechanical properties of the samples at the upper, middle, and bottom of the section.

### 2.3. Simulations

Molecular dynamics (MD) simulations: A 15 Å (radius) iron sphere with an initial velocity ( $V_0$ ) was applied to simulate the impact of LSMMP based on the following equations:[18, 19]

$$P^2(\tau) = mI_0\alpha / 2\tau(\alpha + 1) \quad (1)$$

$$V_0 = 2P(\tau)\tau / m \quad (2)$$

where  $I_0$  is the nominal laser intensity,  $\tau$  the pulse duration,  $m$  the mass of iron sphere,  $P$  the pressure generated during laser irradiation, and  $\alpha$  the factor to account for the increase of plasma thermal energy by the absorbing laser irradiation. A typical velocity of 1 km s<sup>-1</sup> was applied and other speed cases are also calculated for reference. CoCrFeNi HEAs and the iron sphere are single crystals with FCC and Body-centered cubic (BCC) structures respectively. Their lattice constants are 3.56 Å and 2.863 Å. The modified embedded atom method (MEAM) was used in the calculation. Potential

function by Mi et al.[20] was used for HEAs in this simulation. NVT ensemble was applied and the melt area warmed up to 2000 K with a 0.001 ps time step.

A three-dimensional numerical model of the interaction between the laser and the melt pool was used to predict the temperature and flow fields during the LSMMP process. To simplify the calculations, the following assumptions are put forward: 1. The plasma and metal vapor are ideal gases; 2. The effect of the shielding gas on the additive process is ignored. 3. Computational fluids are laminar and Newtonian incompressible fluids.

Conservation equations: The fluid flow and heat transfer process in the LAM process mainly include the conservation equations of mass, momentum, and energy: [21, 22].

Conservation of mass:

$$\frac{\partial}{\partial t}(\rho) + \nabla(\rho \vec{V}) = 0 \quad (3)$$

Conservation of momentum :

$$\frac{\partial}{\partial t}(\rho \vec{V}) + \nabla(\rho \vec{V} \vec{V}) = \nabla(\mu \nabla \vec{V}) - \nabla P - \frac{\mu}{K} \vec{V} + \rho g \quad (4)$$

Conservation of energy :

$$\frac{\partial}{\partial t}(\rho h) + \nabla(\rho \vec{V} h) = \nabla(k \nabla T) \quad (5)$$

where  $\rho$  is the fluid density,  $V$  the fluid velocity,  $t$  the time;  $\mu$  the fluid viscosity,  $P$  the pressure,  $K$  the isotropic permeability,  $g$  the gravity;  $T$  the temperature,  $h$  the material enthalpy, and  $k$  the thermal conductivity.

The laser heat source was set as Gaussian volume heat source model:[23]

$$q_{laser} = \frac{9\alpha_{abs}Q}{\pi R_0^2 H(1-e^{-3})} \exp\left[\frac{-9(x^2 + y^2)}{R_0^2 \log(H/z)}\right] \quad (6)$$

where  $Q$  is laser power,  $H$  the height of the laser heat source,  $\alpha_{abs}$  the absorption rate of the material to the laser heat source, and  $R_0$  the effective radius of the laser beam. More than 95% of the total energy of the laser beam is concentrated in the area with  $R_0$  as the radius.

Driving force: For recoil pressure, a widely accepted model is expressed by:[24]

$$P_r \cong 0.54P_0 \exp\left(\Delta H_{LV} \frac{T - T_{LV}}{RTT_{LV}}\right) \quad (7)$$

where  $P_0$  is the atmospheric pressure,  $R$  the universal gas constant,  $\Delta H_{LV}$  the vaporization enthalpy of the liquid metal,  $T_{LV}$  the liquid-gas equilibrium temperature of the material under a certain pressure,  $\Delta V_{LV}$  the difference between the specific volumes of liquid and gas, and  $V_{LV}$  the specific volume of the gas. The surface tension can be expressed as a function of temperature:[21]

$$\gamma = \gamma_0 + \frac{d\gamma}{dT}(T - T_0) \quad (8)$$

Marangoni force formed on the surface of fluid which can be expressed by:[21]

$$F_{\gamma-i} = -\frac{\partial \gamma}{\partial T} \frac{\partial T}{\partial x_i} \quad (9)$$

where  $T$  is the liquid surface temperature,  $T_0$  the reference temperature,  $\gamma_0$  the surface tension at  $T_0$  temperature,  $F_{\gamma-i}$  the Marangoni force formed by the surface tension gradient in  $i$  direction,  $\gamma$  the surface tension, and “-” indicates that the direction of the force is opposite to the gradient direction of the surface tension.

Pulse pressure: The pulse pressure is the force formed by the nanosecond laser shock impacting on the surface of the melt pool in the vertical direction, and its direction is vertically downward. The shock pressure was simulated as follows:[25, 26]

$$P_{arc} = \frac{P}{2\pi\sigma_p^2} \exp\left(-\frac{r^2}{2\sigma_p^2}\right) \quad (10)$$

where  $r$  is the nominal influenced radius,  $\sigma_p$  the pressure distribution parameter,  $P$  the nominal pressure.

The temporal distribution of the pressure is set to be much larger than the actual laser shock (10 ns scale), due to the limitations of the calculation time and resources.

Geometric model and boundary conditions: As shown in Fig.2 and Video 1 (Supplementary material), the computational domain is  $50\text{ mm} \times 7\text{ mm} \times 10\text{ mm}$  with a grid resolution of  $0.15\text{ mm}$ .  $5\text{ mm}$  fluid region represents the HEAs material and a  $5\text{ mm}$  void region represents the atmospheric environment which was used to capture the free surface. CW laser moves from left to right at the speed of  $8\text{ mm/s}$ . The pulsed laser was applied five times (which can be increased according to needs). They are 1-1.01s, 2-2.01s, 3-3.01s, 4-4.01s, and 5-5.01s respectively. For each boundary, the energy and pressure boundary balance conditions are required. The implicit SOR and VOF algorithms were used to obtain and update free surfaces through self-defined functions, and boundary conditions were imposed on meshes until the end of the calculation.

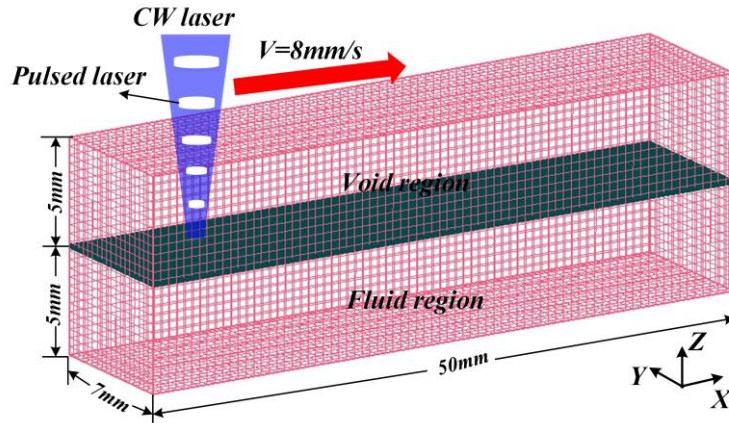


Fig.2. The schematic diagram of computational domain.

### 3. Results and discussion

#### 3.1. Surface topography

To explore the evolution of LSMMP, real-time images of the melt pool under the two processes were collected as shown in Fig. 3 and Video 2 (Supplementary material). Fig. 3(a) records the real-time process of the melt pool in the SLM process. CW laser input fully melts the CoCrFeNi powder and

gradually converges into a plump melt pool in the front of the solidification zone. In the LSMMP process, the melt pool exhibits different characteristics. In Fig. 3(b), the plasma clusters induced by the pulsed laser are observed. The most important thing is that the pulsed laser drives and changes convection in the melt pool through the shock wave. In the transient process of 3.12 ms, melt pool violently oscillates which leads the calm convective state of the melt pool to be transformed into a rolling state. At 3.87 ms, the heat source center of the melt pool becomes exposed to the air and the surface area of melt pool expands after each laser shock, which is beneficial for the heat transfer of the melt pool.

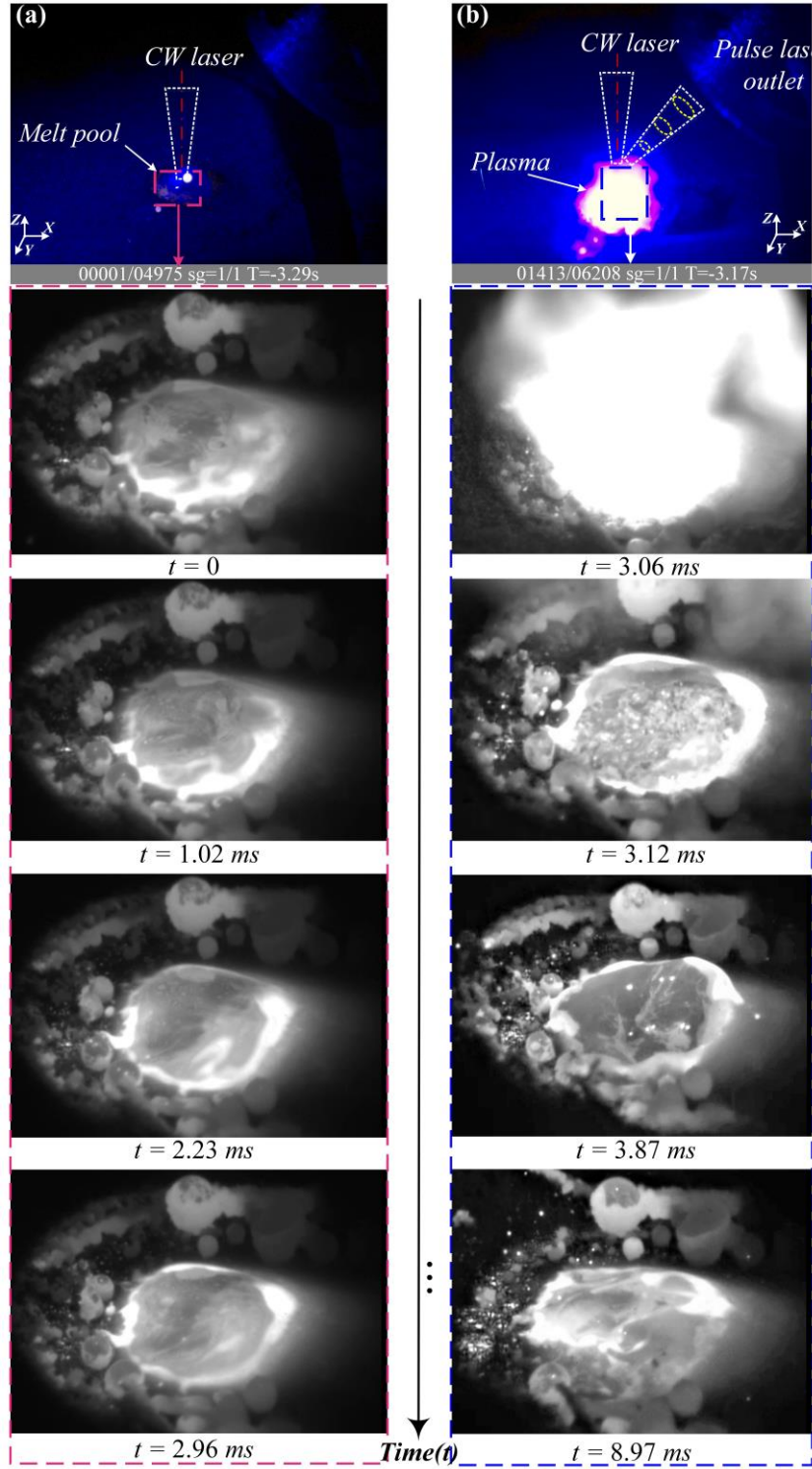


**Fig.3.** Real-time images of melt pool evolution: (a) SLM treatment; (b) LSMMP treatment.

Then, the surface tension makes the melt pool return to its original state to wait for the next pulsed laser.

As a result, this changes its solidified shape. 3D profile data also confirms this result. CW laser input

fully melts the CoCrFeNi powder and it results in an arc-shaped melt pool as shown in Fig. 4(b). This

causes the heat in the melt pool to dissipate slowly. Comparing with Fig. 4(c), the most striking feature of the LSMMP process is that the profile of the melt pool has changed and the size of the melt pool has become wide and flat. This does not damage the additive process. On the contrary, this phenomenon indirectly indicates that the cooling rate of the being shaken melt pool is increased and it solidified before returning to its original arc-shaped state in Fig. 4(b).

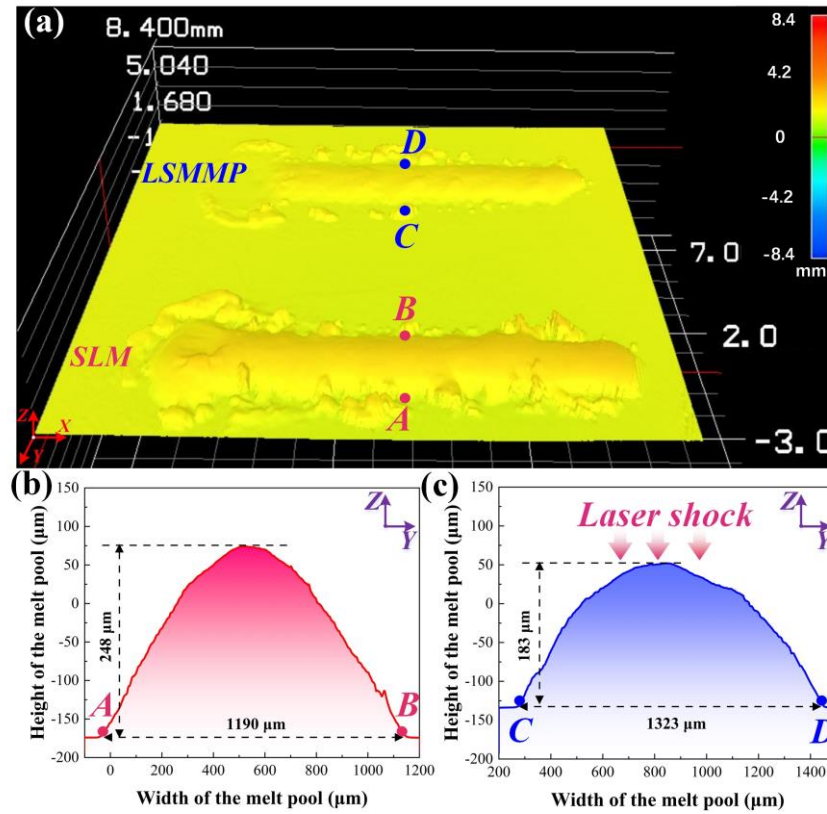


**Fig.4.** 3D topography and section profile of melt pool under different processes: (a) SLM and LSMMP 3D profiles; (b) SLM treatment; (c) LSMMP treatment.

### 3.2. Evolution of material flow and temperature fields

Changes in melt pool morphology contribute to changes of the cooling rate. In the CoCrFeNi HEAs model, a plump melt pool that occurs in the front of the solidification zone, was established to simulate the process of melt pool evolution at the atomic level as shown in Fig. 5(a) and (b). Fig. 5(c) shows the liquid melt pool oscillates after being stressed around. Obvious deformation occurs at the top. The shock wave propagates in three-dimensional directions and the melt pool quickly recovers to its

original state. Similar results also appeared from the cross-sectional analysis of the melt pool. The size of the melt pool is different from that of the SLM model as shown in Fig. 5(b) and (c). And after cooling, the shape becomes wide and flat. Changes in the melt pool profile in the MD also agree with the 3D profile data of the real sample. This demonstrates the effectiveness of the MD simulations on the understanding of the basic mechanism of the LSMMP process. The cooling process under different time steps is shown in Fig. A1 (Supplementary material).

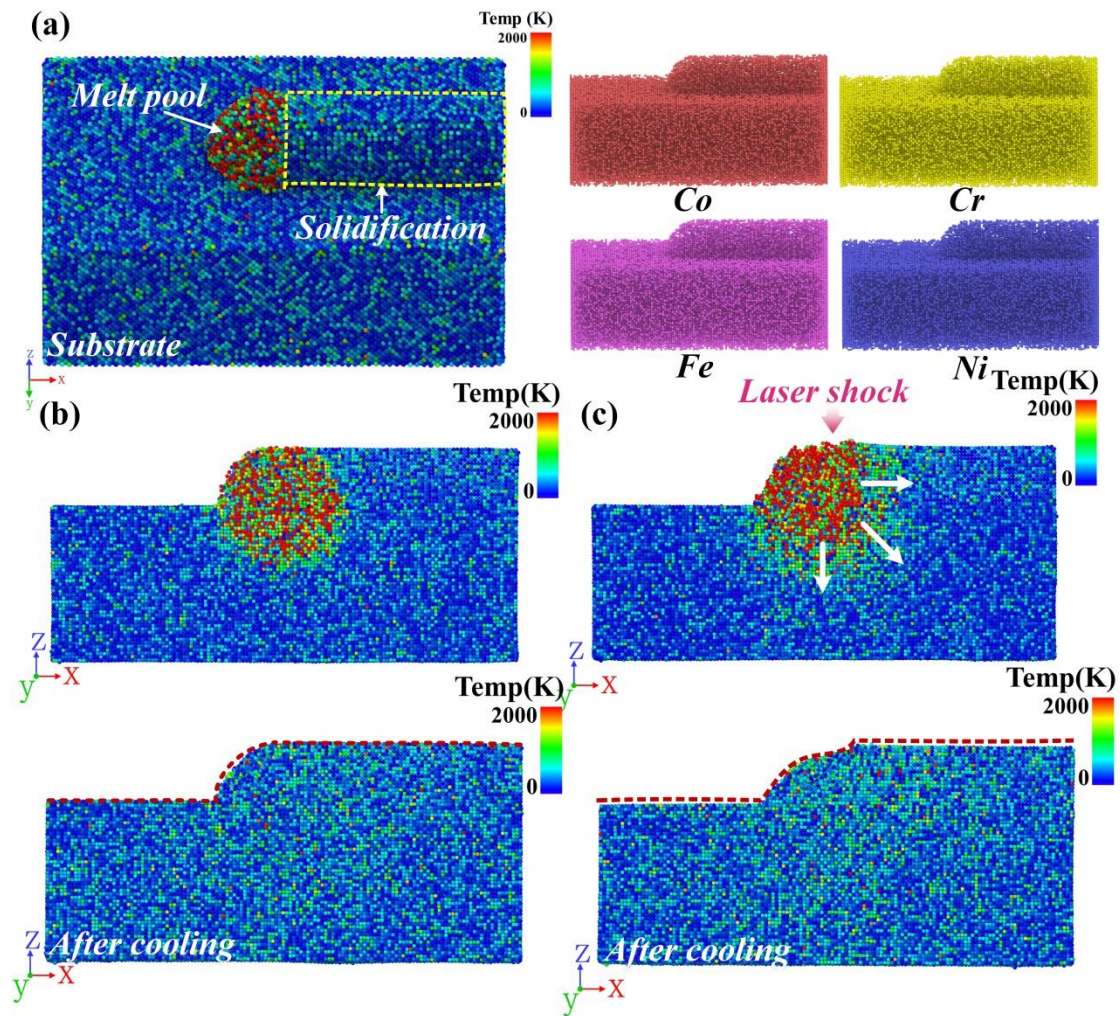


**Fig.5.** Melt pool evolution based on Molecular Dynamics: (a) melt pool model; (b) SLM treatment; (c) LSMMP treatment.

The evolution of material flow is understood from two perspectives. From a microscopic perspective, the movement of atoms inside the melt pool is accelerated after being forced, which is one of the reasons for the increased cooling rate. Liu et al.[27] used the Mean Square Displacement (MSD)

to study the motion of atoms in a system:

$$MSD = \frac{1}{N} \sum_i^N [r_i(t + \Delta t) - r_i(t)]^2 \quad (11)$$

where  $r_i(t)$  represents the position of atom  $i$  at time  $t$ ,  $N$  the number of atoms in the system, and  $\Delta t$  represents the change in time step. Fig.6 shows the MSD curves of atoms in the melt pool region under the two processes. An MSD vector of three quantities dx, dy, and dz in the LSMMP is much larger than SLM as shown in Fig.6 (a). Atoms inside liquid melt pool oscillate after being stressed and spread around. The MSD has an obvious jump and forms a linear relationship with time at the initial stage when the pulsed laser acts on the melt pool as shown in Fig.6 (b), indicating that the movement ability of the atoms is particularly strong at this time. As the temperature decreases, the atoms in the melt pool area begin to arrange in a regular and orderly manner. When the solidification temperature is reached, the MSD curves tend to be horizontal. They formed a regular arrangement with slight oscillations around their equilibrium positions. More results of MSD under different shock cases are shown in Fig. A2. (Supplementary material) These demonstrate the violent convections inside the liquid pool of LSMMP.

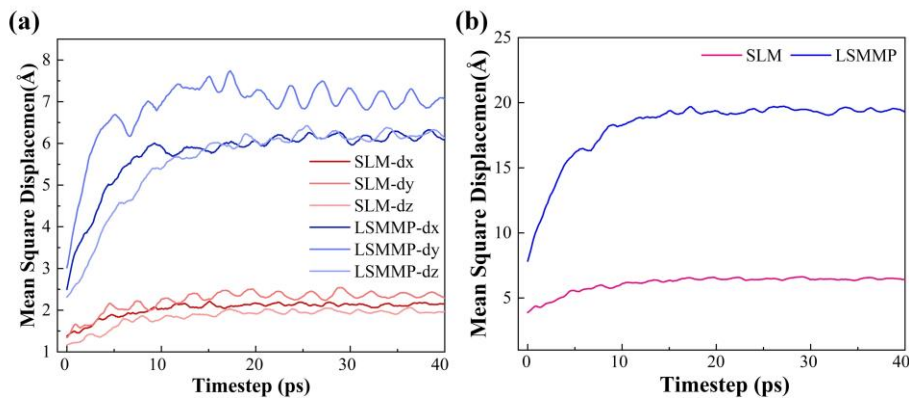


**Fig.6.** The MSD of atoms in the melt pool, (a) the squared dx,dy,dz directions displacements, (b) the total squared displacement.

From a macro perspective, the melt pool is driven and accelerated to flow by the force generated from the laser shock, which adds to the increased cooling rate. The internal melt pool was simulated to

understand it as shown in Fig.7. The CW laser energy input forms nonuniform distribution of the temperature fields of the melt pool, and an asymmetrical convection ring appears inside the plump liquid melt pool. Then it surges from both sides of the melt pool to the surface, forming a typical Marangoni effect. Khairallah et al.[28] demonstrated the significant effect of the recoil pressure and Marangoni convection in laser powder bed fusion. However, the heat source stays on the top surface and lower region is not directly influenced as shown in Fig.7 (a), which is one of the reasons why high thermal stress is always present. This problem is partially solved due to the assistance of pulsed lasers. It can be observed from Fig.7 (b) that the depression appears in the top region because of the applied force. The original symmetrical convective ring is changed and forms multiple convective loops at the top and bottom regions, which accelerate the flow and promote heat to be transported quickly.

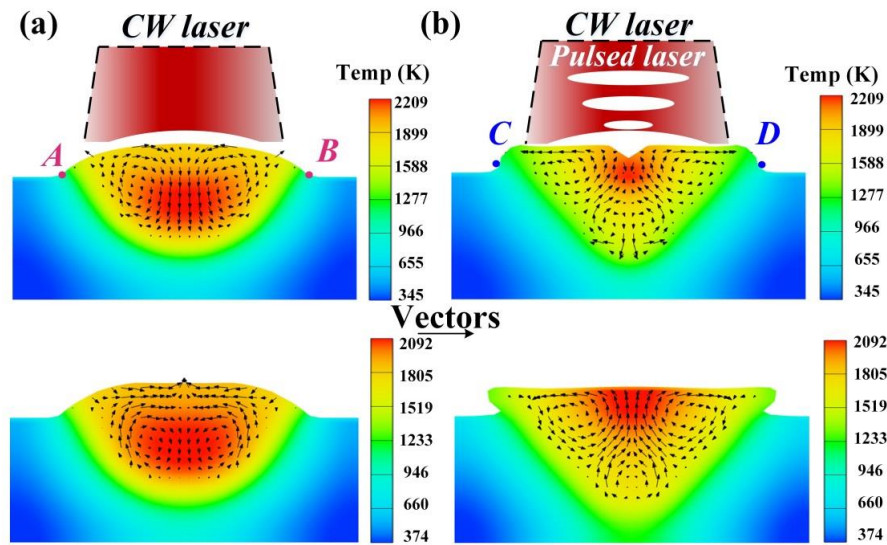


**Fig.7.** Computed temperature and vectors distribution under different processes: (a) SLM treatment; (b) LSMMP treatment.

Although both the accelerated motion of atoms and generation of multiple convection mechanisms suggest the cooling rate of the melt pool after shocking is affected, changes in the cooling rate and the relationship between the different positions inside the melt pool are still not clear. Gan et al. and Karayagiz et al. [29, 30] studied the temperature gradient  $G$ , solidification velocity  $R$  and the cooling rate  $C$  ( $C=G R$ ) in the LAM process, which determined the size of the grain after solidification of the

material and the value of  $G/R$  determined the type of grain growth. Therefore, the temperature gradient  $G$  and the solidification velocity  $R$  were extracted separately as shown in Fig. 8. The melt pool schematics with blue lines demonstrating the representative locations of  $G$  and  $R$  predictions are also included for each case. At different locations of the melt pool: Top, Middle, and Bottom, the same is that in both cases the maximum  $G$  appears at the bottom of the melt pool (with a low solidification velocity  $R$ ), while the minimum  $G$  appears at the top of the melt pool (with a high solidification velocity  $R$ ) as shown in Fig. 8 (a) and (b). The difference is that both  $G$  and  $R$  inside the melt pool under LSMMP increased at different positions. In Fig.8 (c), the average cooling rate  $C$  ( $G \cdot R$ ) was calculated along the centerline of melt pool. From bottom to top, they are 475.7, 207.7, 176.3, and 164.9 K/s under SLM while 562.9, 412.5, 329.3, and 371.2 K/s under LSMMP. They are both increased regardless of the location in the melt pool and indicate that LSMMP treatment is beneficial for increasing the cooling rate. The average value of  $G/R$  is calculated along the centerline of melt pool as shown in Fig.8 (d). From bottom to top they are 578.9, 221.6, 98, and 38.2 under SLM while 520.1, 225.8, 80.5, and 17.4 under LSMMP. The value of  $G/R$  in SLM is greater than LSMMP, which leads to different grain growth types at different locations of the melt pool.

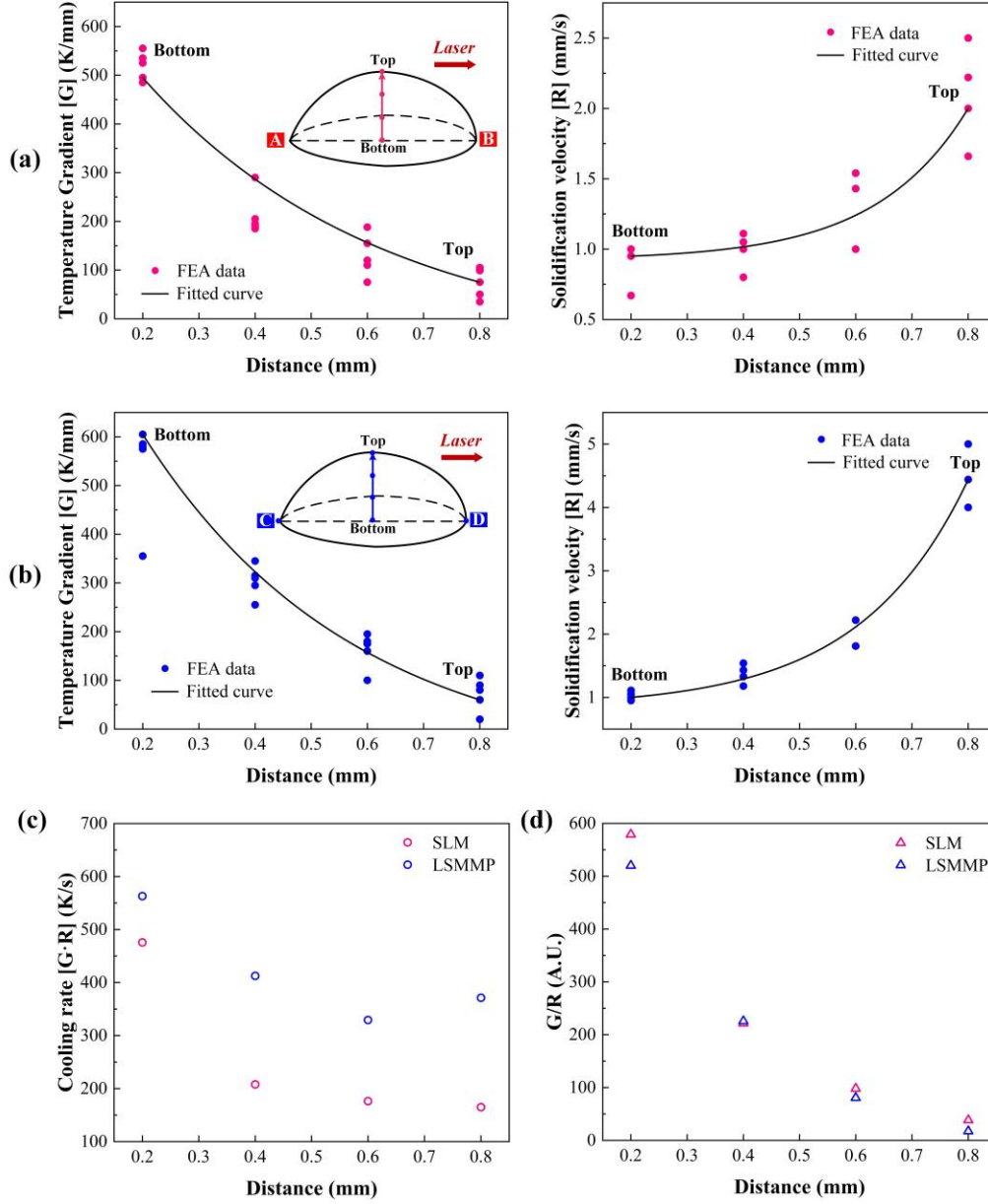
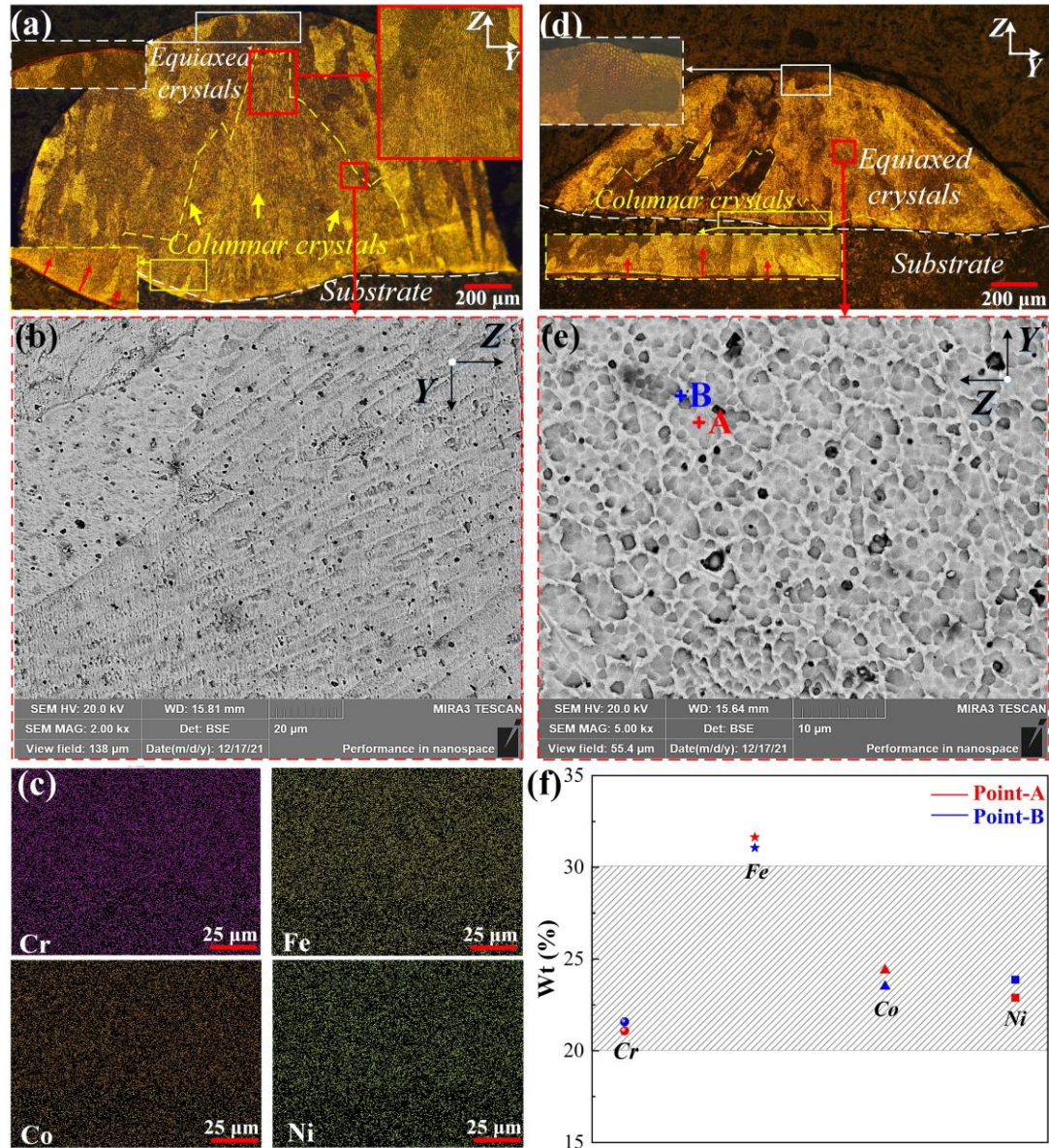


Fig.8. The predicted temperature gradient,  $G$  and solidification velocity,  $R$  along the centerline of melt pool are shown for two sets of process: (a) SLM; (b) LSMMP. The melt pool schematics with blue lines demonstrating the representative locations of  $G$  and  $V$  predictions are also included for each case; (c) cooling rate ( $G \cdot R$ ), and (d) the value of  $G/R$  under two treatments.

### 3.3. Microstructure analysis

To verify the results in the simulation, microstructures under different treatments were collected as shown in Figure 9. Under the SLM process, the cross-section of the melt pool shows a non-equilibrium structure composed of columnar dendrites and equiaxed dendrites as shown in Fig. 9(a). From the local bottom boundary enlarged view of the melt pool, there is a good bond between the HEA and the substrate, indicating that the formed sample has a good tensile ability. Columnar dendrites are observed

at the bottom of the melt pool and grow upward perpendicular to the substrate boundaries. Lin et al.[31] also found columnar dendrites are one of the typical features of LAMed HEAs. In the LAM process, the laser irradiation area is in the center and the edge area of melt pool belongs to the cooling zone. A high-temperature gradient  $G$  is formed between them, which drives the columnar dendrites to grow upward along the temperature gradient from the bottom of the melt pool as shown in Fig.9(b). Furthermore, the solid and liquid lines (S/L) inside the melt pool are promoted to show a directional solidification trend from the inside to the outside and the bottom to the top. When it is reaching the middle and upper region of the melt pool, a lower  $G$  due to the closer distance from the heat source cannot drive the epitaxial growth of columnar dendrites. At the same time, the EDS results of the columnar dendrites in Fig. 9(b) area show that Cr, Fe, Co, and Ni elements are uniformly distributed in the sample as shown in Fig.9(c).



**Fig.9.** Samples under SLM treatment: (a) The microstructure of the melt pool section, (b) The local SEM image of columnar crystals, (c) The EDS result of in (b); Samples under LSMMP treatment: (d) The microstructure of the melt pool section, (e) The local SEM image of equiaxed crystal, (f) The EDS result of points A and B in (e).

In Fig. 9(d) and (e), it is found that the growing columnar dendrites become equiaxed dendrites in the middle and top regions of melt pool. A Columnar-Equiaxed Transition (CET) occurs. The liquid melt pool oscillates from top to bottom after being stressed and spreads out to form multiple convective loops inside the melt pool as shown in Fig.10 (a). The microstructure relationship between the temperature gradient  $G$  and solidification velocity  $R$  is crucial and is shown in Fig.10 (b). LSMMP decreases the value of  $G/R$ , making it smaller than that of SLM in the middle and top regions of the

melt pool. Therefore, the recrystallization mode changes to equiaxed dendrite growth. In addition, a high cooling rate can also result in the nucleation rate of the grains increasing, which is also beneficial for the formation of small equiaxed dendrites.

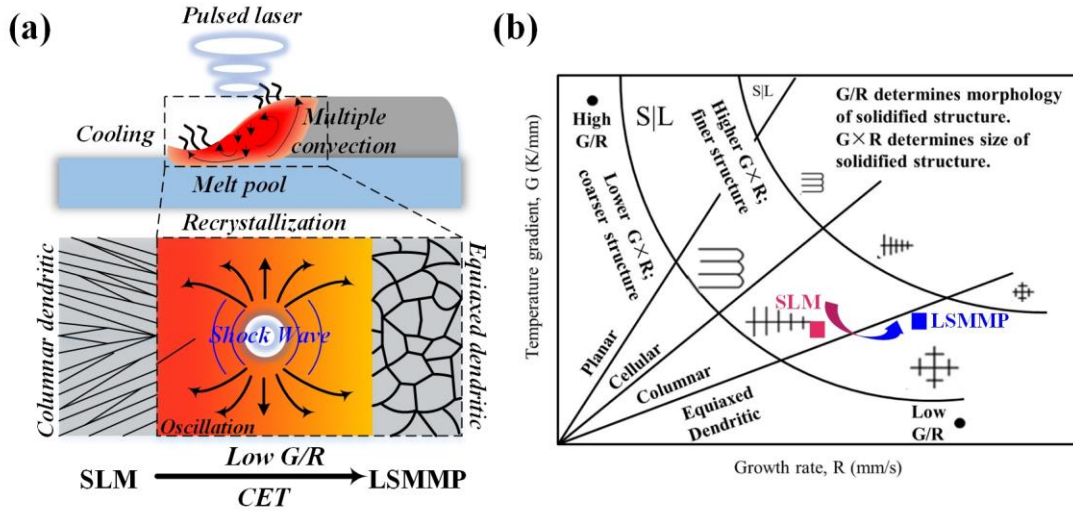


**Fig.10.** (a) Columnar-Equiaxed Transition (CET) occurs in LSMMP treatment, (b) Microstructure selection map for solidification morphology as a function of G and R.[29]

In Fig. 9(f), each element of CoCrFeNi accounts for about 25% and the shaded area represents a reasonable distribution. The dendrite point A and the interdendritic point B exhibit equal elemental content of Co, and Ni, and the Cr element is slightly lower. Only the content of Fe element is slightly out of range, which is attributed to a large amount of mixing of HEAs with the substrate. A reduction in the content of other elements also contributes to this result. Abolkassem et al.[32] showed the formation of Cr phase clusters and  $\text{Cr}_2\text{O}_3$ , leading to the reduction of Cr elements during the forming process, while other Cr, Co, and Ni elements are likely to form solid solutions with Fe. Figure 11 shows the XRD patterns of CrFeCoNi powder and CrFeCoNi HEAs under different processes. The three typical peaks of the FCC structure, namely (111), (200), and (220), dominate in the range from  $20^\circ$  to  $90^\circ$ , and the results show that a stable FCC structure is achieved through all processing conditions. Besides, Co also forms a BCC solid solution with Fe. Abolkassem et al.[32] also obtained similar

results.

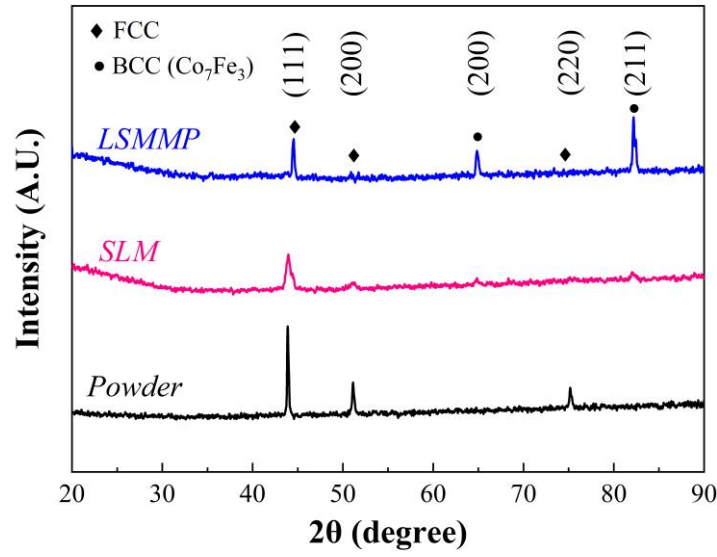
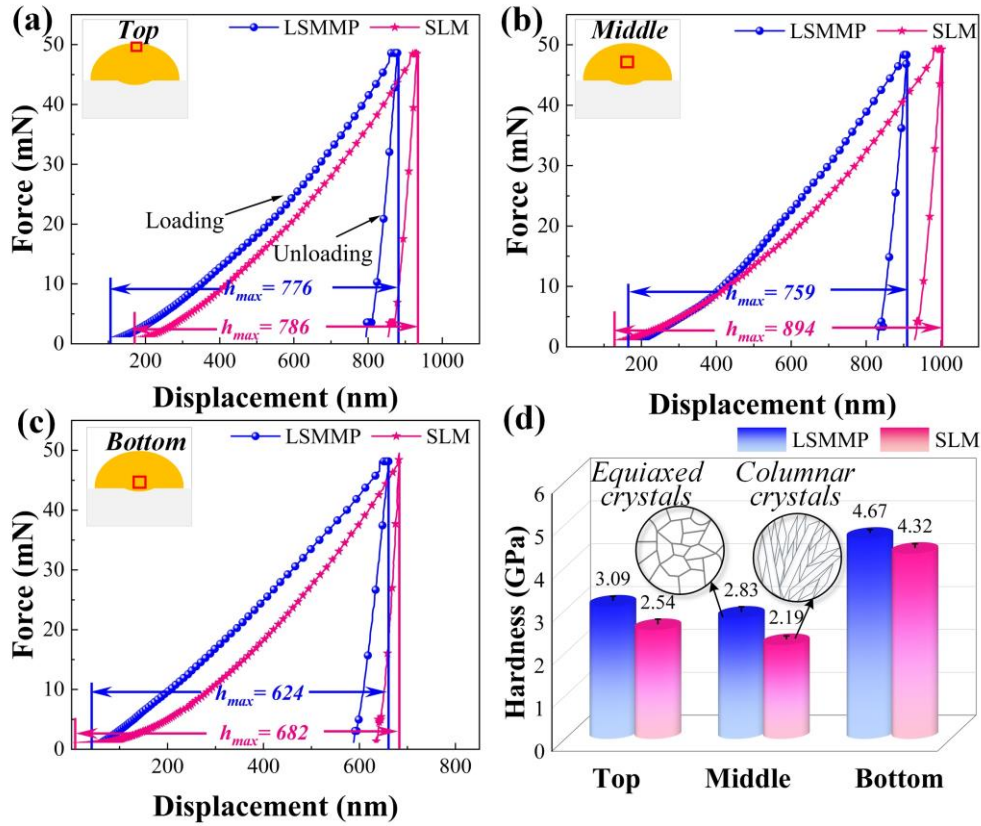


Fig.11. X-Ray Diffraction patterns of samples under different treatments.

### 3.4. Nano-indentation analysis

Changes in microstructure directly affect the mechanical properties of materials. Under the same experimental loading conditions, the nanoindentation results show that different positions inside the melt pool also exhibit different displacements. In Fig.12 (a), (b), and (c), the displacements of the top, middle, and bottom regions of the melt pool after LSMMP treatment are 776 nm, 759 nm, and 624 nm respectively, which are smaller than those of 786 nm, 894 nm, and 682 nm after SLM treatment, respectively. It indicates that the deformation resistance of the material is improved. The grain structures inside the melt pool under LSMMP are equiaxed dendrites while those of SLM are columnar dendrites. Under the same load, the isotropic characteristics of equiaxed dendrites are significantly stronger than that of columnar dendrites in terms of deformation resistance. At the bottom of melt pool, the opposite trend occurs that the deformation resistance is stronger than the middle and top regions respectively. The results of nano-hardness show the top, middle, and bottom of the melt pool after LSMMP treatment are 3.09GPa, 2.83GPa, and 4.67GPa respectively as shown in Fig.12 (d), which are all better than those of 2.54GPa, 2.19GPa, and 4.32GPa after SLM treatment. It also indicates that the

CET under LSMMP brings beneficial improvements to mechanical properties.



**Fig.12.** Nanoindentation load-displacement in different areas: (a) Top, (b) Middle, and (c) Bottom area of melt pool; (d) Hardness in different areas.

#### 4. Conclusions

A new LSMMP method that utilizes LSP on the liquid melt pool was studied. By combining numerical simulation and experimental studies to understand the action mechanism between laser shock and melt pool, the new process was systematically verified from the three perspectives of forming process: processes, microstructures, and mechanical properties. The results showed an effective in-situ modulative tool for controlling the additive manufacturing process, and some important conclusions are summarized as follows:

1. The convection mechanism of the melt pool in LSMMP is revealed. The plasma induced by the pulsed laser acts on the melt pool, which promotes the transformation of melt pool flow mode from the Marangoni effect to a multi-convective loop and successfully increases the cooling rate by accelerating

melt pool flow.

2. The microstructure evolution law of CrFeCoNi HEAs is obtained. After the action of the pulsed laser, the growth rate of the melt pool is increased and the microstructures undergo CET transformation.

3. Non-destructive real-time fabrication of CrFeCoNi HEAs with stable FCC structures is realized. The nano-hardness of the top, middle and bottom regions of melt pool is improved and no segregation defects occur.

### **CRedit authorship contribution statement**

**Heng Lu:** Investigation, Visualization, Integration, Writing-Original draft. **Xiaohan Zhang:** Resources. **Jian Liu:** Resources. **Shusen Zhao:** Resources and supervision. **Xuechun Lin:** Resources and supervision. **Hui Li:** Resources and supervision. **Yaowu Hu:** Conceptualization, Methodology, supervision, Funding acquisition.

### **Acknowledgments**

This work was supported by the National Natural Science Foundation of China (Grant No. 51901162). The authors thank the support of the National Talent Program of China.

### **Declaration of Competing Interest**

The authors declare that they have no known competing financial interests or personal relationships that could have influenced the work reported in this paper.

### **Appendix A. Supplementary material**

This document provides supplementary information to “Study on laser shocking of melt pool in Laser Additive Manufacturing of FeCoCrNi High-Entropy Alloys”

#### **1. Cooling process**

The Molecular Dynamics (MD) simulation of the Laser Shock Modulation of Melt Pool (LSMMP) has five stages: relax, heating (2000K), constant temperature annealing, shocking, and cooling. Before entering the cooling stage, the shocking module is removed to observe the liquid surface oscillation process. The total step of the cooling is 40 ps as shown in Fig.A1, and the SLM process has no shock module. The liquid melt pool oscillates after being stressed. The shock wave propagates in three-dimensional directions as shown in Fig.A1(b). At 4 ps, the oscillated melt pool diffuses to the solid phase and the substrate. At 20 ps, the temperature of the melt pool decreases and begins to gradually solidify. After cooling, the shape of SLM model has no significant changes. The shape of LSMMP model does not recover to a similar state that of SLM and becomes flat. Changes in the melt pool profile also agree with the 3D profile data. This phenomenon indirectly indicates that the cooling rate of the being shaken melt pool is increased.

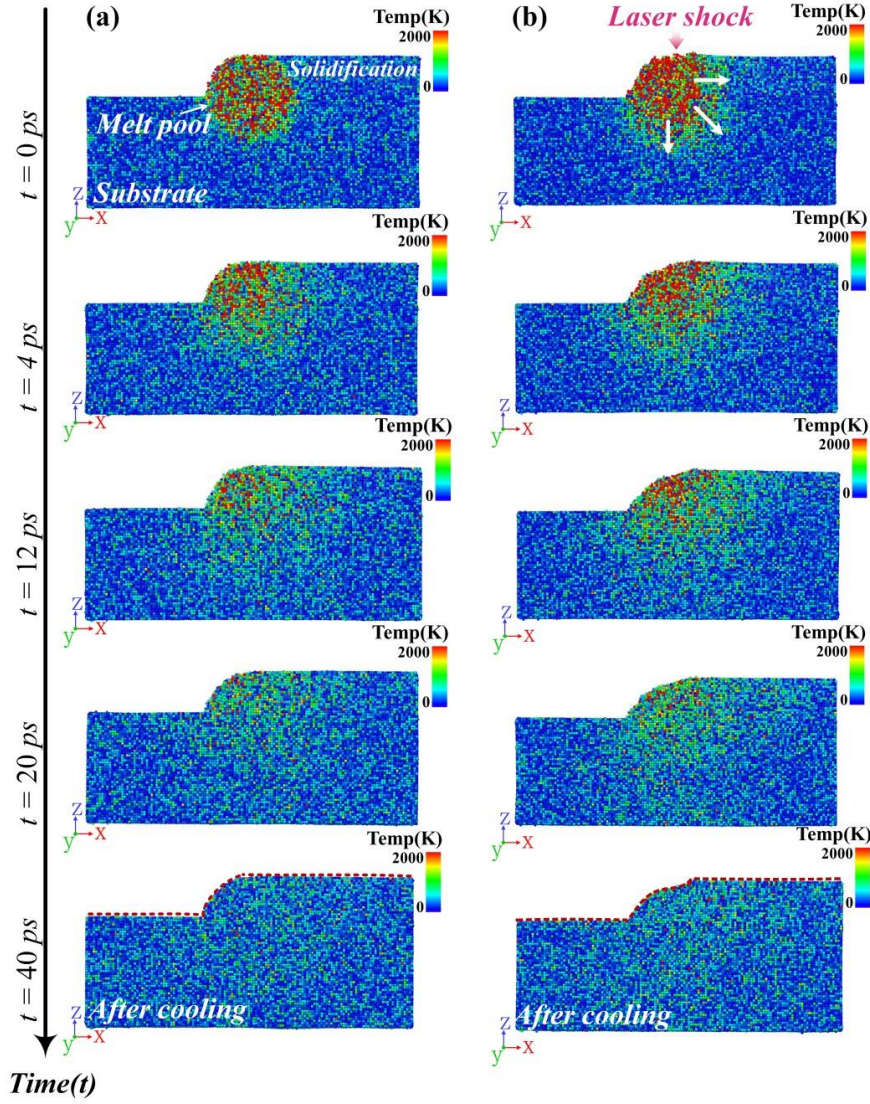


**Fig.A1.** The cooling process of melt pool based on Molecular Dynamics: (a) SLM treatment; (c) LSMMP treatment.

## 2. Different shock cases.

More shock cases including impact velocities of 1.5, 2, and 2.5 km/s are simulated as shown in Fig.A2 (a). The results show that there are no more benefits when a larger shock wave acts on the melt pool. It does not work if the shock wave is too small and destroys the melt pool if the shock wave is too large. In our previous experiments, the laser energy density of  $S_{LED}=93.59 \text{ J/cm}^2$  makes a beneficial oscillation effect. This is the case of the velocity of 1 km in MD. At this time, the MSD of the atoms in the melt pool is the largest and indicating that the atomic movement ability is particularly strong which accelerates the escape of the heating source. However, the other MSD curve is less than the case of

1km. An MSD vector of three quantities involving dx, dy, and dz is also displayed as shown in Fig.A2.

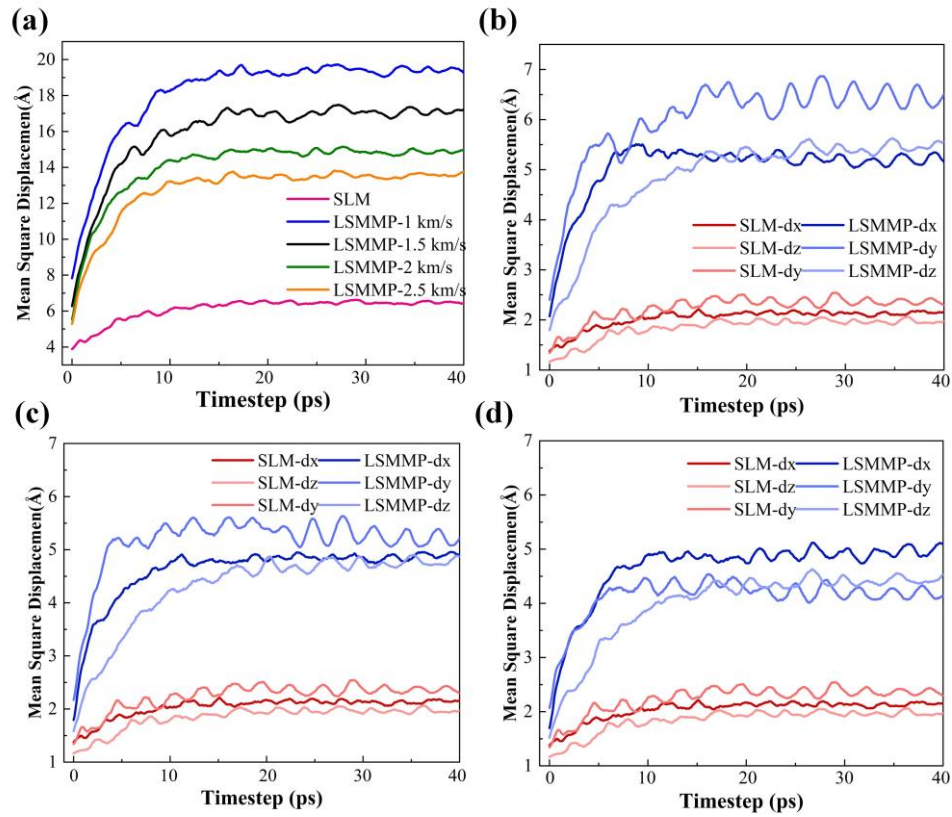


**Fig.A2.** The MSD of atoms in the melt pool, (a) total squared displacement under different shock conditions; the squared dx,dy,dz directions displacements: (b) 1.5 km/s, (c) 2 km/s, and (d) 2.5 km/s.

## References

- [1] J.W. Yeh, S.K. Chen, S.J. Lin, J.Y. Gan, T.S. Chin, T.T. Shun, C.H. Tsau, S.Y. Chang, Nanostructured High-Entropy Alloys with Multiple Principal Elements: Novel Alloy Design Concepts and Outcomes, *Advanced Engineering Materials*. 6 (5) (2004) 299-303. <https://doi.org/10.1002/adem.200300567>.
- [2] Y. Brif, M. Thomas, I. Todd, The use of high-entropy alloys in additive manufacturing, *Scripta Materialia*. 99 (2015) 93-96. <https://doi.org/10.1016/j.scriptamat.2014.11.037>.
- [3] A. Ostovari Moghaddam, N.A. Shaburova, M.N. Samodurova, A. Abdollahzadeh, E.A. Trofimov, Additive manufacturing of high entropy alloys: A practical review, *Journal of Materials Science &*

Technology. 77 (2021) 131-162. <https://doi.org/10.1016/j.jmst.2020.11.029>.

- [4] R. Li, P. Niu, T. Yuan, P. Cao, C. Chen, K. Zhou, Selective laser melting of an equiatomic CoCrFeMnNi high-entropy alloy: Processability, non-equilibrium microstructure and mechanical property, Journal of Alloys and Compounds. 746 (2018) 125-134. 10.1016/j.jallcom.2018.02.298.
- [5] R. Zhou, Y. Liu, C. Zhou, S. Li, W. Wu, M. Song, B. Liu, X. Liang, P.K. Liaw, Microstructures and mechanical properties of C-containing FeCoCrNi high-entropy alloy fabricated by selective laser melting, Intermetallics. 94 (2018) 165-171. <https://doi.org/10.1016/j.intermet.2018.01.002>.
- [6] W. Hu, Z. Yu, Y. Lu, J. Huo, Z. Qin, X. Lu, R.L. Narayan, Enhanced plasticity in laser additive manufactured Nb-reinforced bulk metallic glass composite, Journal of Alloys and Compounds. 918 (2022) 165539. <https://doi.org/10.1016/j.jallcom.2022.165539>.
- [7] Z.G. Zhu, Q.B. Nguyen, F.L. Ng, X.H. An, X.Z. Liao, P.K. Liaw, S.M.L. Nai, J. Wei, Scripta Materialia. 154 (2018) 20-24. <https://doi.org/10.1016/j.scriptamat.2018.05.015>.
- [8] F. Peyrouzet, D. Hachet, R. Soulas, C. Navone, S. Godet, S. Gorsse, Correction to: Selective Laser Melting of Al<sub>0.3</sub>CoCrFeNi High Entropy Alloy: Printability, Microstructure, and Mechanical Properties, Jom. 72 (10) (2020) 3705-3705. 10.1007/s11837-020-04149-w.
- [9] C. Zhang, K. Feng, H. Kokawa, B. Han, Z. Li, Cracking mechanism and mechanical properties of selective laser melted CoCrFeMnNi high entropy alloy using different scanning strategies, Materials Science and Engineering: A. 789 (2020) 139672. <https://doi.org/10.1016/j.msea.2020.139672>.
- [10] P. Niu, R. Li, S. Zhu, M. Wang, C. Chen, T. Yuan, Hot cracking, crystal orientation and compressive strength of an equimolar CoCrFeMnNi high-entropy alloy printed by selective laser melting, Optics & Laser Technology. 127 (2020) 10.1016/j.optlastec.2020.106147.

- [11] Q. Jiang, P. Zhang, Z. Yu, Y. Tian, S. Ma, AlCoCrFeNi high entropy alloy fabricated via selective laser melting reinforced by Fe-based metallic glass, *Materials Letters*. 307 (2022) 10.1016/j.matlet.2021.130994.
- [12] J. Li, H. Chen, S. Li, Q. Fang, Y. Liu, L. Liang, H. Wu, P.K. Liaw, Tuning the mechanical behavior of high-entropy alloys via controlling cooling rates, *Materials Science and Engineering: A*. 760 (2019) 359-365. <https://doi.org/10.1016/j.msea.2019.06.017>.
- [13] Z. Tong, X. Ren, J. Jiao, W. Zhou, Y. Ren, Y. Ye, E.A. Larson, J. Gu, Laser additive manufacturing of FeCrCoMnNi high-entropy alloy: Effect of heat treatment on microstructure, residual stress and mechanical property, *Journal of Alloys and Compounds*. 785 (2019) 1144-1159. <https://doi.org/10.1016/j.jallcom.2019.01.213>.
- [14] C. Knowles, T. Becker, R. Tait, The effect of heat treatment on the residual stress levels within direct metal laser sintered Ti-6Al-4V as measured using the hole-drilling strain gauge method, 2012.
- [15] Z. Tong, H. Liu, J. Jiao, W. Zhou, Y. Yang, X. Ren, Improving the strength and ductility of laser directed energy deposited CrMnFeCoNi high-entropy alloy by laser shock peening, *Additive Manufacturing*. 35 (2020) 101417. <https://doi.org/10.1016/j.addma.2020.101417>.
- [16] Y. Hu, Y. Xuan, X. Wang, B. Deng, M. Saei, S. Jin, J. Irudayaraj, G.J. Cheng, Superplastic Formation of Metal Nanostructure Arrays with Ultrafine Gaps, *Adv. Mater.* 28 (41) (2016) 9152-9162. <https://doi.org/10.1002/adma.201602497>.
- [17] Y. Hu, P. Kumar, R. Xu, K. Zhao, G.J. Cheng, Ultrafast direct fabrication of flexible substrate-supported designer plasmonic nanoarrays, *Nanoscale*. 8 (1) (2016) 172-182. 10.1039/C5NR06899A.

- [18] Y. Hu, Y. Xuan, X. Wang, B. Deng, M. Saei, S. Jin, J. Irudayaraj, G.J. Cheng, Superplastic Formation of Metal Nanostructure Arrays with Ultrafine Gaps, *Adv Mater.* 28 (41) (2016) 9152-9162. 10.1002/adma.201602497.
- [19] R. Fabbro, J. Fournier, P. Ballard, D. Devaux, J. Virmont, PHYSICAL STUDY OF LASER-PRODUCED PLASMA IN CONFINED GEOMETRY, *JOURNAL OF APPLIED PHYSICS.* 68 (2) (1990) 775-784. 10.1063/1.346783.
- [20] W.-M. Choi, Y.H. Jo, S.S. Sohn, S. Lee, B.-J. Lee, Understanding the physical metallurgy of the CoCrFeMnNi high-entropy alloy: an atomistic simulation study, *npj Computational Materials.* 4 (1) (2018) 10.1038/s41524-017-0060-9.
- [21] L. Shi, X. Li, L. Jiang, M. Gao, Numerical study of keyhole-induced porosity suppression mechanism in laser welding with beam oscillation, *Science and Technology of Welding and Joining.* 26 (5) (2021) 349-355. 10.1080/13621718.2021.1913562.
- [22] W. Huang, H. Wang, T. Rinker, W. Tan, Investigation of metal mixing in laser keyhole welding of dissimilar metals, *Materials & Design.* 195 (2020) 10.1016/j.matdes.2020.109056.
- [23] H. Wang, Y. Shi, S. Gong, Numerical simulation of laser keyhole welding processes based on control volume methods, *J. Phys. D: Appl. Phys.* 39 (21) (2006) 4722-4730. 10.1088/0022-3727/39/21/032.
- [24] J.Y. Lee, S.H. Ko, D.F. Farson, C.D. Yoo, Mechanism of keyhole formation and stability in stationary laser welding, *J. Phys. D: Appl. Phys.* 35 (13) (2002) 1570-1576. 10.1088/0022-3727/35/13/320.
- [25] C.S. Wu, K. Tsao, Modelling the three-dimensional fluid flow and heat transfer in a moving weld pool, *Engineering Computations.* 7 (1990) 241-248. 10.1108/eb023811.

- [26] M.L. Lin, T.W. Eagar, Pressures produced by gas tungsten arcs, *Metallurgical Transactions B*. 17 (3) (1986) 601-607. 10.1007/BF02670227.
- [27] P. Liu, E. Harder, B.J. Berne, On the Calculation of Diffusion Coefficients in Confined Fluids and Interfaces with an Application to the Liquid–Vapor Interface of Water, *The Journal of Physical Chemistry B*. 108 (21) (2004) 6595-6602. 10.1021/jp0375057.
- [28] S.A. Khairallah, A.T. Anderson, A. Rubenchik, W.E. King, Laser powder-bed fusion additive manufacturing: Physics of complex melt flow and formation mechanisms of pores, spatter, and denudation zones, *Acta Materialia*. 108 (2016) 36-45. <https://doi.org/10.1016/j.actamat.2016.02.014>.
- [29] Z. Gan, G. Yu, X. He, S. Li, Numerical simulation of thermal behavior and multicomponent mass transfer in direct laser deposition of Co-base alloy on steel, *International Journal of Heat and Mass Transfer*. 104 (2017) 28-38. 10.1016/j.ijheatmasstransfer.2016.08.049.
- [30] K. Karayagiz, L. Johnson, R. Seede, V. Attari, B. Zhang, X. Huang, S. Ghosh, T. Duong, I. Karaman, A. Elwany, R. Arróyave, Finite interface dissipation phase field modeling of Ni–Nb under additive manufacturing conditions, *Acta Materialia*. 185 (2020) 320-339. 10.1016/j.actamat.2019.11.057.
- [31] D. Lin, X. Xi, X. Li, J. Hu, L. Xu, Y. Han, Y. Zhang, L. Zhao, High-temperature mechanical properties of FeCoCrNi high-entropy alloys fabricated via selective laser melting, *Materials Science and Engineering: A*. (2021) 10.1016/j.msea.2021.142354.
- [32] S.A. Abolkassem, L.Z. Mohamed, G.A. Gaber, O.A. Elkady, Microstructure and corrosion behavior of FeNiCoCrCu and FeNiCoCrMn high entropy alloys manufactured by powder metallurgy in different acid media, *Journal of Materials Research and Technology*. 10 (2021)

1122-1142. 10.1016/j.jmrt.2020.12.016.